**PAPER**

# A novel optical method for measuring 3D full-field strain deformation in geotechnical tri-axial testing

IOP Publishing Measurement Science and Technology
Meas. Sci. Technol. **31** (2020) 015403 (15pp) https://doi.org/10.1088/1361-6501/ab3c80

# A novel optical method for measuring 3D full-field strain deformation in geotechnical tri-axial testing

**Pengpeng Wang[1,2], Yong Sang[3,5,6], Xiaoxia Guo[1,2], Longtan Shao[1,2], Jianlong Zhao[3] and Xiaomeng Ji[4]**

[1] State Key Laboratory of Structural Analysis for Industrial Equipment, Dalian University of Technology, Dalian City, Liaoning Province 116024, People's Republic of China
[2] Department of Engineering Mechanics, Dalian University of Technology, Dalian City, Liaoning Province 116024, People's Republic of China
[3] School of Mechanical Engineering, Dalian University of Technology, Dalian City, Liaoning Province 116024, People's Republic of China
[4] State Key Laboratory of Coastal and Offshore Engineering, Dalian University of Technology, Dalian City, Liaoning Province 116024, People's Republic of China

E-mail: sang110@163.com and sangyong@dlut.edu.cn

Received 11 April 2019, revised 18 August 2019
Accepted for publication 19 August 2019
Published 21 October 2019

**Abstract**

Soil is a complex multiphase material and has anisotropic properties; meanwhile, soil behaviour is typically evaluated in tri-axial testing. Until now, there have still been some challenges in measuring the total strain, the local strain deformation and the volume changes during tri-axial testing. In conventional geotechnical testing, it cannot acquire enough deformation characteristics. To improve the situation, a digital image measurement system has been constructed and calibrated on a geotechnical tri-axial apparatus. In the digital image measurement system, the three-dimensional digital image correlation (3D-DIC) technique was applied to measure the soil specimen's 3D large deformation and reconstruct the 3D surface topography of the specimen. To improve the measurement accuracy, a standard spatial calibration procedure to rectify the 3D reconstruction data in tri-axial testing is proposed to improve the effect of the projective transformation in stereovision. Through rectification, the root-mean-squared error in terms of displacement measurement in the tri-axial testing was reduced by more than half. Furthermore, a subpixel edge detector was applied to estimate the volume changes based on the 3D-DIC results. Finally, comparing the results between the image measurement system and the conventional measurement method, the proposed method not only can obtain the specimen's distribution of 3D full-field deformation, volume strain and so on, but also can provide a method for rectifying the 3D data measured by the image measurement technique in tri-axial testing. The results from 3D reconstruction can describe directly the characteristics of anisotropy and non-uniformity in geotechnical materials. The results can provide more information than conventional testing when establishing a constitutive model in soil mechanics.

Keywords: geotechnical tri-axial apparatus, 3D-DIC, 3D full-field deformation, subpixel edge detector, volume strain

(Some figures may appear in colour only in the online journal)

[5] Author to whom any correspondence should be addressed.
[6] School of Mechanical Engineering, Dalian University of Technology, No.2, Ling Gong Road, Dalian City, Liaoning Province, 116024, People's Republic of China

 

## 1. Introduction

Digital image correlation (DIC) is a non-contact digital image recognition technology based on dense point tracking. This technique is very suitable for the measurement of the deformation field. Since two-dimensional digital image correlation (2D-DIC) was invented in the 1980s [1, 2], many optimization algorithms have been proposed to improve its computational efficiency, matching robustness, and accuracy [3–9]. In the 2D-DIC technique, several subsets with sufficient intensity variations are selected from the reference image. Then, the DIC technique tracks these deformed subsets by searching the deformed image based on a predefined criterion, such as a correlation function. The fundamental principle of 2D-DIC has been described in detail in other studies [10, 11]. Pan *et al* [3] combined an efficient inverse compositional matching strategy, a Gauss–Newton (IC-GN) algorithm, and the robust zero-mean normalized sum of squared difference (ZNSSD) correlation criterion to improve the computational efficiency and matching robustness, and the efficiency was approximately three to five times faster than the traditional methodology. ZNSSD correlation is insensitive to the scale and offset changes in lighting fluctuations [12]. Currently, IC-GN and ZNSSD have been used as a common parameter optimization method and correlation criterion, respectively. Furthermore, due to its advantages, 2D-DIC has been applied in many fields for full-field deformation and shape measurements [13–17]. However, 2D-DIC has typically been used to measure the predominant in-plane or small out-of-plane motion, and it cannot be applied in the curved surface measurement or out-of-plane motion. To expand the application of DIC, three-dimensional (3D) DIC has been developed, which is based on the 3D reconstruction of the stereovision system and the tracking algorithm of the 2D-DIC [18]. The 3D-DIC technique is also widely used in 3D deformation field measurement [4, 19–22]. In conventional geotechnical testing, tri-axial testing is a common method used to study the mechanical properties of soil. Because soil typically has obvious local failure deformation due to progressive failure, the changes in the soil specimen are measured by some sensors during the testing, for example, load cells, pressure sensors, displacement sensor and so on. However, the local deformation field cannot be obtained quantitatively by these sensors. Some researchers have applied the 3D-DIC technique to measure the 3D full-field deformation in the geotechnical testing accurately. Medina-Cetina and Rechenmacher [23] measured the full-field deformations using 3D-DIC to improve the predictive ability of computational soil mechanics. Tang *et al* [24] explored the effects of the confining pressure on the progressive failure behaviours of rocks using 3D-DIC with six cameras. The 3D-DIC method can obtain the full-field strains and crack evolution of the specimen. Higo *et al* [25] quantitatively obtained the displacement field over the entire Toyoura sand specimen using image analysis of the x-ray computed tomography (CT) images using the DIC technique during tri-axial compression under drained conditions. However, these measurement results typically lack the calibration process of the 3D-DIC measurement system during these tests. In general, the fundamental principle of the DIC method can be classified broadly as either 2D-DIC or 3D-DIC. However, the measurement system accuracy in 3D-DIC is more complex than 2D-DIC. First, the lens distortion and the results of the stereo calibration would affect the accuracy of the measurement results. Second, because two cameras are used, the same regions from the left and right images have obvious differences in terms of the view angles. The correlation of the DIC method between two views would be weakened. At the same time, the soil is known to be a granular material. The processes of preparing a soil specimen and the experiments are more complex than that of metal specimens. The complex apparatus would also affect image quality. Third, the recorded global axial strain of the specimen would exceed 14% in the geological tri-axial testing. Because of the anisotropic properties of the soil materials, the local deformation may be several times larger than the global deformation [26]. The correlation would also be weakened progressively during the testing. Therefore, many aspects influence the accuracy of 3D-DIC measurements. Sometimes, in order to use the image measurement system, geotechnical testing must be simplified [23, 27]. In conventional DIC algorithms, the reference image is typically the initial image. It is nearly impossible to trace larger local deformations for the reference image using a conventional DIC algorithm. This shortcoming is the so-called decorrelation effect. To overcome the 'decorrelation effect', Song *et al* [27] updated the reference images for every 4th image, i.e. every 0.2% of the axial strain, and then, the incremental displacements were computed. The large deformation of soil specimen was measured using this method. Due to frequent updates of the reference images, this method would lead to larger cumulative errors. Pan *et al* [28] proposed an incremental reliability-guided digital image correlation (RG-DIC) to maintain the accuracy of the large deformation, and this method reduces the number of reference images updates. Using this method, several seed points are pre-defined in the original reference image. If all correlation coefficients of the seed points exceed the pre-set threshold, the reference images would be updated. This method perfectly solves the problem of DIC large deformation measurement.

To improve the accuracy of 3D-DIC in geotechnical tri-axial testing, in this paper, a novel tri-axial experiment measuring apparatus and rectification method for 3D data were developed based on an image measurement system to implement complex geotechnical experiments. For measuring 3D large deformations, the incremental RG-DIC method was applied to the 3D-DIC. Most importantly, a standard spatial calibration procedure using stereovision is proposed to improve the effectiveness of the projective transformation in stereovision. A series of consolidated drained tri-axial tests were carried out on Hainan (China) sand specimens. The 3D deformation was obtained using the proposed 3D-DIC methods, and the results were rectified using the proposed spatial calibration procedure. Based on the rectified results, the local failure and the shape changes of the soil specimens were analysed quantitatively. At the same time, combining the subpixel edge detector, a method for estimating the volume strain is proposed. Finally, comparing the results between

the image measurement system and conventional measurement method, the proposed method was shown to be effective and had more advantages than the conventional experimental method, for example, in the specimen's distribution of the local deformation and the local volume strain. The results can provide more information to aid in the establishment of the constitutive model in soil mechanics.

The remainder of the paper is organized as follows. The next section describes the experimental apparatus and the experimental condition. Section 2 describes the components of the experimental apparatus, the condition of the experimental sands and the realization of the 3D-DIC. Section 3 describes the proposed calibration procedure and the calibration results. The section 4 presents the measurement results using the proposed method, and the subpixel edge detector was applied to obtain the volume strain. Finally, section 5 presents the conclusions of the paper.

## 2. Experimental methodology

### *2.1. Experimental apparatus and digital image measurement system*

In the field of geotechnical engineering testing, to simulate the depth condition of the soil, the apparatus used to measure the properties of geotechnical materials is different form that used to measure conventional solid materials, for example, metal and concrete. The tri-axial testing would be applied to geotechnical test, which is different from the uniaxial tensile or compression test of universal material testing machine. The schematic diagram of the experimental apparatus for the tri-axial testing is shown in figure 1. The soil specimen wrapped in a latex membrane was placed into the sealed chamber. The chamber was filled with a pressurized fluid. This fluid can be compressed air, water or oil. The pressurized fluid provides the confining pressure for the specimen to simulate the soil depth because the strength of the soil varies with the soil depth. This kind experiment is known as a tri-axial experiment in geotechnical engineering testing. Compressed air was used as the pressurized fluid to capture the specimen image with little distortion in these experiments. The confining pressure was achieved using an air pump and controlled by an electromagnetic proportional air pressure valve because water and oil have higher refractive indexes, which leads to specimen image distortion [29]. Under a specific confining pressure, the specimen is compressed directly by the axial loading rod. The strength in the confining pressure can be measured by the load cells. According to the diagram in figure 1, the electro-hydraulic servo static-dynamic tri-axial apparatus was designed by the State Key Laboratory of Structural Analysis for Industrial Equipment at Dalian University of Technology. The apparatus was primarily composed of a hydraulic pressure station servo valve, a servo-hydraulic cylinder, an air pump, an air pressure valve, sensors, a digital camera system, a data acquisition (DAQ) system and the control algorithms system. In this instrument, the tracking control strategy of the electro hydraulic servo system was based on an adaptive fuzzy sliding mode controller. For the static loading experiment, the displacement tracking error was less than 0.003 mm. For the dynamic loading experiment, the maximum cyclic frequency could reach 20 Hz. Additionally, an image measurement system was applied to capture the deformation of the specimens. The displacement of the actuator was measured using a linear variable differential transformer (LVDT). The force was measured by the inner load cell. The confining pressure and the specimens' volume change were measured by the pressure transducer and the differential pressure cell, respectively.

The experimental apparatus is shown in figure 2(a). The axial load cell was installed in the pressure chamber to decrease the effect of friction. The pressure chamber was redesigned to bear 1 MPa of pressure, and one pane of tempered glass was installed in the front of the pressure chamber to capture the deformation images. To avoid light reflection of an external light source, two sets of LED lights were installed in the pressure chamber to provide a stable light source. The image acquisition system of two CCD cameras was placed in front of the pressure chamber to capture the loading process, as shown in figure 2(b). The initial synchronization between the image acquisition system and the load command was established by an external synchronization trigger signal. This synchronization function was very useful for the automatic control system (ACS) to improve the measurement accuracy. A schematic diagram of the stereo digital image measurement system is depicted in figure 2(c). In these tri-axial tests, all specimens were compressed with a slow loading rate. Images were acquired every 5 s using two 14-bit Pike F-100B/C (1000 × 1000 pixels) digital cameras which were made by allied vision technologies (AVT) in Germany. Two cameras having different view angles captured 2D images of the same object area. According to the triangulation principle and bundle adjustment, a reconstruction 3D structure was realized.

### *2.2. Experimental procedure and specimen preparation*

The experiment materials were the sand material from Hainan (China) province and the fly ash generated during the combustion of coal for energy production from Jilin (China) province. The average sand particle size is 0.089 mm, while the average fly ash particle size is 0.159 mm. All the specimens were constructed using a standard cylindrical mould 61.8 mm in diameter and 125 mm in height with subsequent vibratory compaction methods. The fully saturated sand specimens were prepared by displacing the air in the specimen by $CO_2$ for two hours and then passing de-aired water, while the fly ash specimens would be placed in airless water in vacuum condition for tens of days to reach the saturation. All the experiments were divided into four groups for the consolidated drained tri-axial compression test, as recommended by ASTM D7181-11 [30]. In every group, the specimens had approximately the same test conditions to verify the reproducibility of the tests. The sand material from Hainan province was used in the first three groups of tests, and the test names were called 'HnCD' test. While the fly ash from Jilin province was used in the fourth group of tests, the test names were called 'JLCD' test.

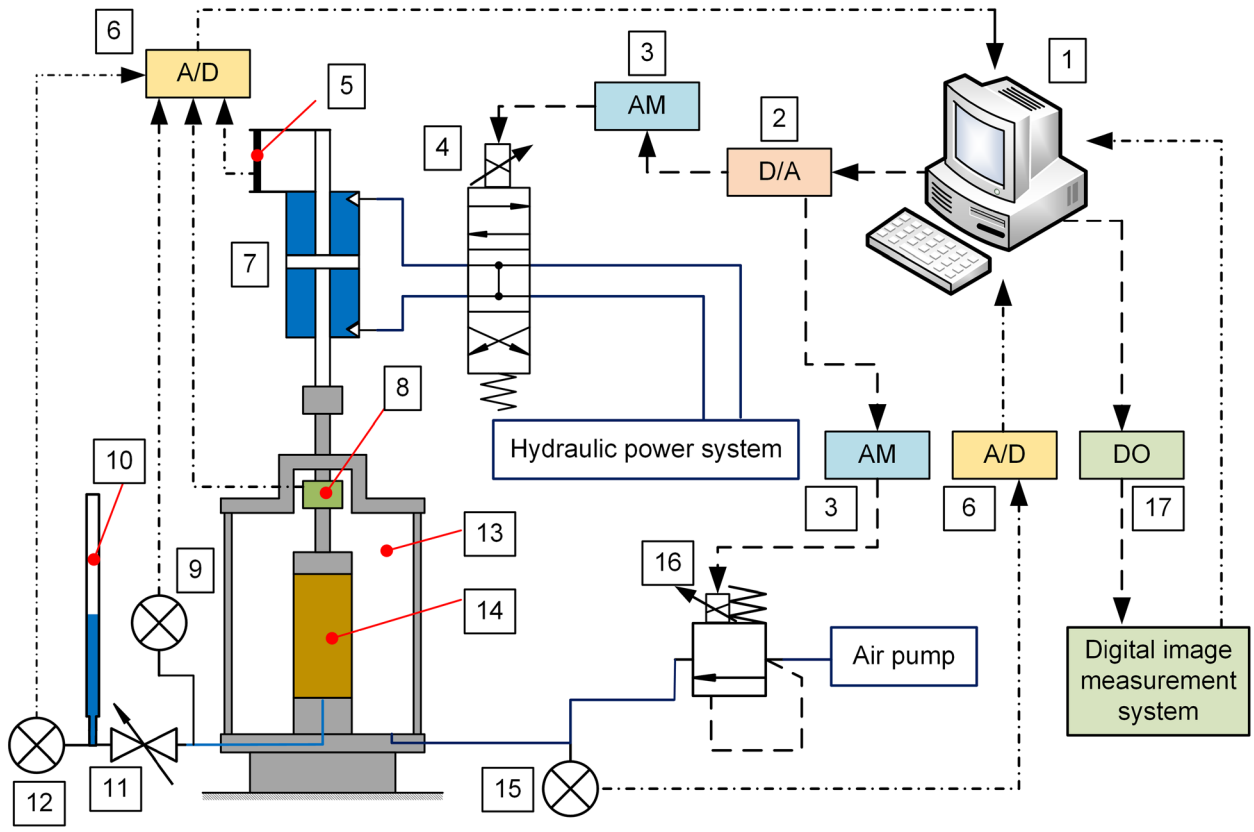


**Figure 1.** Diagram of the experimental apparatus. 1- Controlling computer; 2- digital/analog converter; 3- amplifier; 4- hydraulic servo valve; 5- LVDT; 6- analog/digital converter; 7- double acting servo cylinder; 8- load cell; 9- pore pressure transducer; 10- volume change burette; 11- switch valve; 12- differential pressure cell; 13- pressure chamber; 14- soil specimen; 15- pressure transducer; 16- relieve valve; 17- digital output port.

According to the specimen's initial relative density: $D_r$ in soil mechanics, the soil physical state can be divided into the three states: dense soil, medium dense soil and loose soil. When $67\% \leqslant D_r \leqslant 100\%$, the specimen is in a dense state; When $33\% \leqslant D_r < 67\%$, the specimen is in a medium dense state; When $D_r < 33\%$, the specimen is in a loose state. The experimental characteristics of the specimens are shown in table 1 including the test confining pressure, soil physical sate, and so on. All the specimens were sheared at a constant strain rate of 0.2%/min after saturation and consolidation of the specimens. An irregular grayscale value on the specimen surface is required when using the DIC method, such as a speckle pattern or a natural pattern of materials. In this study, because the specimen was wrapped by the membrane, an irregular pattern was created by spraying black and white paint on the membrane until there was an irregular random distribution with high contrast, as shown in figure 2(b). The realization and calibration procedure of the specimen 3D reconstruction will be discussed in detail in the next section.

### 2.3. Realization of 3D-DIC

The 3D-DIC method is based on the stereovision system [19, 31]. The principle of stereovision is shown in figure 2(c). An arbitrary spatial point ($P$) on the object is recorded by the cameras (left camera and right camera) and corresponds two projective points ($P_l$ and $P_r$) in the left and right image plane. Assume that ($x_p$, $y_p$, $z_p$, 1) are the homogeneous coordinates in the world coordinate system for the point (P). ($x_{pl}$, $y_{pl}$, $z_{pl}$, 1) and ($x_{pr}$, $y_{pr}$, $z_{pr}$, 1) represent the homogeneous coordinates corresponding to point ($P$) in the left and the right camera coordinate systems, respectively. Equations (1) and (2) show the transformation equation of point ($P$) from the word coordinate to the camera coordinate system as follows:

$$\begin{bmatrix} x_{pl} \\ y_{pl} \\ z_{pl} \\ 1 \end{bmatrix} = \begin{bmatrix} R_l & T_l \\ 0 & 1 \end{bmatrix} \cdot \begin{bmatrix} x_p \\ y_p \\ z_p \\ 1 \end{bmatrix} \tag{1}$$

$$\begin{bmatrix} x_{pr} \\ y_{pr} \\ z_{pr} \\ 1 \end{bmatrix} = \begin{bmatrix} R_r & T_r \\ 0 & 1 \end{bmatrix} \cdot \begin{bmatrix} x_p \\ y_p \\ z_p \\ 1 \end{bmatrix}. \tag{2}$$

In equations (1) and (2), $R_l$ and $R_r$ are $3 \times 3$ rotation matrixes that rotate the word coordinate system to align with the left and the right camera coordinate system, respectively. $T_l$ and $T_r$ are $3 \times 1$ translation matrixes that translate the world coordinate system to the origin of the left and the right camera coordinate system, respectively.

If $R_l$, $R_r$, $T_l$ and $T_r$ are obtained by equations (1) and (2), the rotation matrix R and translation matrix $T$ from the right camera coordinate system to the left camera coordinate

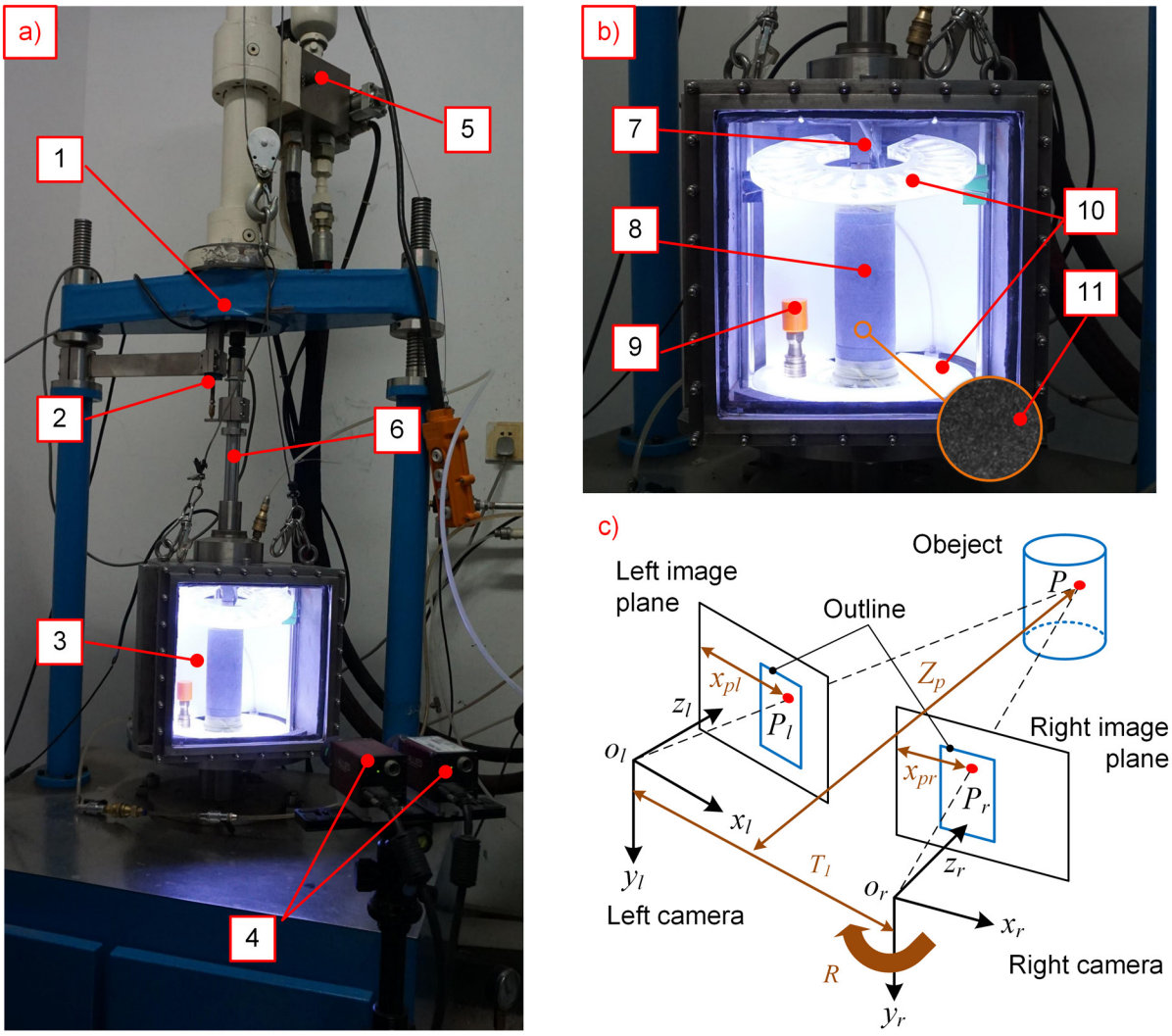


**Figure 2.** (a) The composition of the apparatus. (b) The composition of the pressure chamber. (c) The principle of 3D rectification. 1- The experiment apparatus; 2- LVDT; 3- pressure chamber; 4- stereovision system; 5- hydraulic servo valve; 6- the loading rod; 7- loading cell; 8- soil specimen; 9- the static reference; 10- LED lights; 11- speckle.

**Table 1.** Experimental characteristics of the specimens.

| Group number | Test name | Confining pressure $\sigma_3$ (kPa) | Test conditions[a] | Initial height H (mm) | Initial density $\rho_d$ (g cm$^{-3}$) | Initial relative density $D_r$ (%) | Soil physical state[b] |
|---|---|---|---|---|---|---|---|
| 1 | HnCD-111 | 100 | CD | 124.62 | 1.589 | 76.3 | Dense |
| | HnCD-112 | 100 | CD | 124.20 | 1.593 | 77.3 | Dense |
| | HnCD-113 | 100 | CD | 124.47 | 1.591 | 76.8 | Dense |
| 2 | HnCD-211 | 100 | CD | 124.91 | 1.493 | 47.5 | Medium |
| | HnCD-212 | 100 | CD | 124.65 | 1.515 | 54.4 | Medium |
| | HnCD-213 | 100 | CD | 124.79 | 1.502 | 50.1 | Medium |
| 3 | HnCD-131 | 300 | CD | 124.08 | 1.626 | 86.4 | Dense |
| | HnCD-132 | 300 | CD | 123.58 | 1.583 | 74.4 | Dense |
| | HnCD-133 | 300 | CD | 124.33 | 1.594 | 77.6 | Dense |
| 4 | JLCD-111 | 100 | CD | 125.04 | 0.789 | 62.1 | Medium |
| | JLCD-112 | 100 | CD | 125.02 | 0.772 | 56.2 | Medium |
| | JLCD-113 | 100 | CD | 124.98 | 0.787 | 61.3 | Medium |

[a] CD indicates that the specimen was the consolidated drained tri-axial compression test.
[b] 'Dense' represents that the specimen was in a dense state; 'medium' represents that the specimen was in a medium dense state.

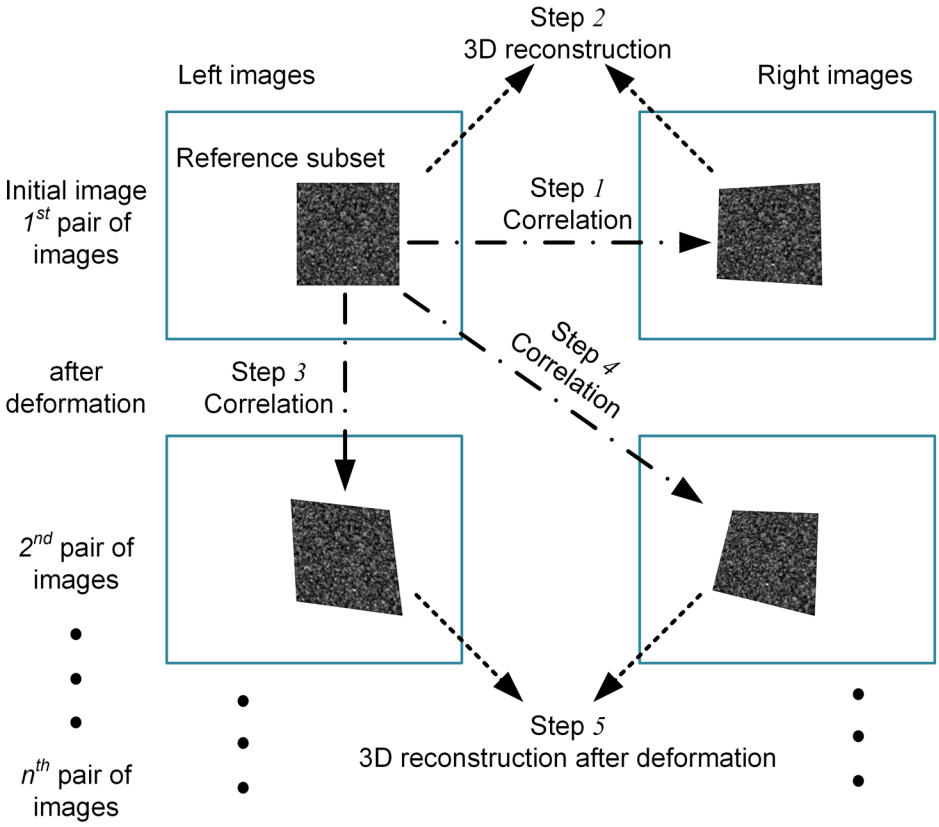


**Figure 3.** Procedure for realizing the tracking and stereo correspondence of 3D-DIC.

system, as shown in figure 2(c), can be obtained by equations (3) and (4) as follows:

$$R = R_{\mathrm{l}} \cdot (R_{\mathrm{r}})^{\mathrm{T}} \tag{3}$$

$$T = T_{\mathrm{l}} - R \cdot T_{\mathrm{r}}. \tag{4}$$

The equations (3) and (4) can be used to realize the stereo calibration procedure. The stereo calibration would be used to align the two cameras into one viewing plane mathematically. In the work, the left camera is used as the primary camera. So, the right camera plane would be aligned into the left camera plane. Then, the spatial position of the point ($P$) in the left camera coordinate systems can be obtained based on the triangle similarity theorems after the stereo calibration procedure, as shown in the following equation (5):

$$\begin{cases} x_{\mathrm{pl}} = \frac{u_{\mathrm{pl}} \cdot T_x}{u_{\mathrm{pl}} - u_{\mathrm{pr}}} \\ y_{\mathrm{pl}} = \frac{v_{\mathrm{pl}} \cdot T_x}{u_{\mathrm{pl}} - u_{\mathrm{pl}}} \cdot \frac{d_{\mathrm{V}}}{d_{\mathrm{H}}} \\ z_{\mathrm{pl}} = \frac{f \cdot T_x}{(u_{\mathrm{pl}} - u_{\mathrm{pr}}) \cdot d_{\mathrm{H}}} \end{cases}. \tag{5}$$

In equation (5), $x_{\mathrm{pl}}$, $y_{\mathrm{pl}}$, $z_{\mathrm{pl}}$ are the spatial position from the point ($P$) in the left camera coordinate systems, in *mm*; $u_{\mathrm{pl}}$ and $u_{\mathrm{pr}}$ are the horizontal coordinates from point ($P$) in the left and the right image views at $P_{\mathrm{l}}$ and $P_{\mathrm{r}}$, in *pixels*; $v_{\mathrm{pl}}$ is the vertical coordinates from point ($P$) in the left image view at $P_{\mathrm{l}}$, in *pixels*; $d_{\mathrm{H}}$ is the horizontal physical length of one pixel in charge-coupled device (CCD) sensor, in *mm*; $d_{\mathrm{V}}$ is the vertical physical length of one pixel in CCD sensor, in *mm*; $f$ is the focal length of the camera, in *mm*; $T_x$ is the horizontal distance from the right camera to the left camera, in *mm*, and it is the horizontal component of $T$ in equation (4).

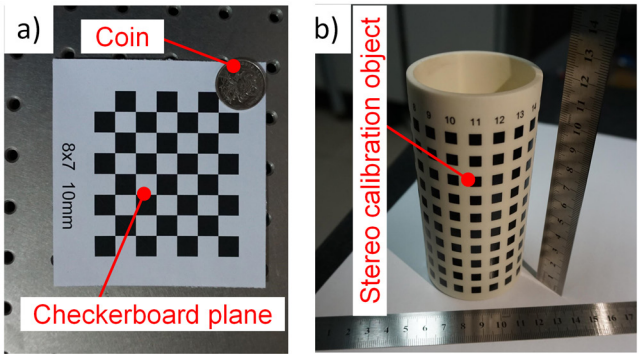


**Figure 4.** Two types of calibration targets and their scale references: (a) checkerboard plane. (b) Stereo calibration object.

In the 3D reconstruction, in addition to tracking the target in the time series, for example, tracking point ($P$), the points or subsets on the object should be matched in the left and right image views at the same time. This is so-called stereo correspondence. Figure 3 presents the procedure to realize the 3D-DIC tracking and stereo correspondence in this paper. The tracking method and the matching method all adopt the ZNSSD coefficient which with a range of [0,4] is intuitive to show the similarity between the undeformed subsets (e.g. reference subsets) and deformed subsets [32], as shown

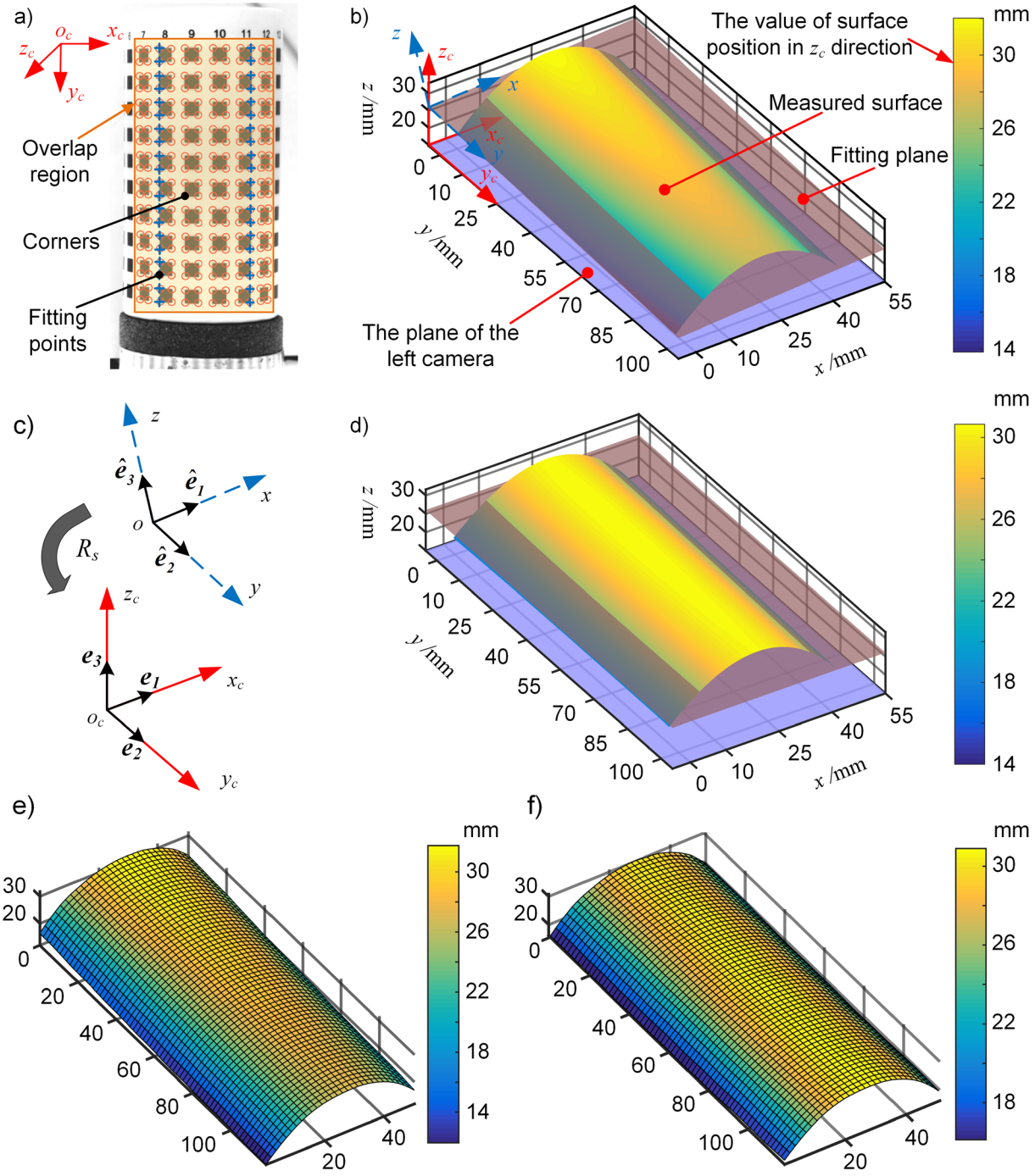


**Figure 5.** The procedure and results of the spatial geometric transformation: (a) the overlap region in the stereo calibration object; (b) 3D reconstruction of the stereo calibration object before rectification; (c) diagram of the coordinate rotation; (d) 3D reconstruction the stereo calibration object after rectification; (e) 3D reconstruction of the initial specimen before rectification; (f) 3D reconstruction of the initial specimen after rectification.

in equations (6)–(10). The smaller the value of $C_{\mathrm{ZNSSD}}$, the better the matching will be. Especially, $C_{\mathrm{ZNSSD}} = 0$ denotes a perfect matching. In the matching procedure, the first image from the left camera is considered to be the reference image, and the other images are deformed images. The deformed subsets in the right image would be matched to the reference image using equations (6)–(10); then, the 3D position can be obtained using equation (5). After completing the first pair of images, the next pair of images would be matched to the reference image. The procedure will loop until processing the

**Table 2.** Some image measurement information and the incline of the specimens.

| Test name | Physical length per pixel (mm/pixel) | Initial Average diameter D (mm) | The three base vectors of the fitting plane relative to the left camera | | |
|---|---|---|---|---|---|
| | | | $\widehat{\boldsymbol{e}}_1$ | $\widehat{\boldsymbol{e}}_2$ | $\widehat{\boldsymbol{e}}_3$ |
| HnCD-111 | 0.1947 | 61.73 | (0.9982, −0.0105, −0.0588) | (0.0133, 0.9988, −0.0476) | (−0.0581, 0.0483, 0.9971) |
| HnCD-112 | 0.1941 | 61.98 | (0.9983, −0.0130, 0.0589) | (0.0040, 0.9989, −0.0476) | (−0.0575, 0.0477, 0.9972) |
| HnCD-113 | 0.1944 | 61.71 | (0.9975, −0.0133, 0.0691) | (0.0166, 0.9987, −0.0474) | (−0.0494, 0.0482, 0.9976) |
| HnCD-211 | 0.1939 | 61.75 | (0.9701, 0.0301, −0.2410) | (−0.0414, 0.9982, −0.0422) | (0.2395, 0.0510,0.9696) |
| HnCD-212 | 0.1911 | 61.50 | (0.9999, 0.0064, 0.0137) | (−0.0053, 0.9971, −0.0758) | (−0.0140, 0.0757, 0.9970) |
| HnCD-213 | 0.1932 | 61.48 | (0.9993, 0.0029, 0.0383) | (−0.0002, 0.9975, −0.0712) | (−0.0383, 0.0711, 0.9967) |
| HnCD-131 | 0.1965 | 61.36 | (0.9988, −0.0094, −0.0476) | (0.0067, 0.9984, −0.0558) | (0.0479, 0.0554, 0.9973) |
| HnCD-132 | 0.1935 | 62.33 | (0.9842, 0.0050, 0.1767) | (0.0036, 0.9988, −0.0483) | (−0.1765, 0.0482, 0.9831) |
| HnCD-133 | 0.1933 | 61.87 | (0.9986, −0.0202, −0.1491) | (0.0281, 0.9983, −0.0514) | (−0.1478, 0.0550, 0.9875) |
| JLCD-111 | 0.1885 | 61.45 | (0.9952, 0.0001, 0.0974) | (0.0056, 0.9983, −0.0584) | (−0.0971,0.0586, 0.9935) |
| JLCD-112 | 0.1918 | 61.83 | (0.9993, −0.0017, −0.0380) | (−0.0010,0.9974, −0.0725) | (0.0382, 0.0725, 0.9966) |
| JLCD-113 | 0.1909 | 61.81 | (0.9985, −0.0007, −0.0548) | (−0.0028, 0.998, −0.0631) | (0.0548, 0.0631, 0.9965) |

last pair of images. To overcome the 'decorrelation effect' for large deformation in tri-axial testing, the incremental RG-DIC method is also applied to the 3D-DIC technique [28]. In the incremental RG-DIC method, a threshold has been preset. The threshold is set as 0.5 in this work. If the $C_{\mathrm{ZNSSD}}$ of the nth pair of images is larger than the pre-set threshold, which means no serious 'decorrelation effect'. Then, the reference image will be replaced with the left image of the $(n-1)$th pair of images:

$$C_{\mathrm{ZNSSD}} = \sum_{i=-M}^{M}\sum_{j=-M}^{M}\left[\frac{f(x_i,y_j)-f_{\mathrm{m}}}{\Delta f} - \frac{g(x_i',y_j')-g_{\mathrm{m}}}{\Delta g}\right]^2 \tag{6}$$

$$f_{\mathrm{m}} = \frac{1}{(2\cdot M+1)^2}\sum_{i=-M}^{M}\sum_{j=-M}^{M} f(x_i,y_j) \tag{7}$$

$$\Delta f = \sqrt{\sum_{i=-M}^{M}\sum_{j=-M}^{M}\left[f(x_i,y_j)-f_{\mathrm{m}}\right]^2} \tag{8}$$

$$g_{\mathrm{m}} = \frac{1}{(2\cdot M+1)^2}\sum_{i=-M}^{M}\sum_{j=-M}^{M} g(x_i',y_j') \tag{9}$$

$$\Delta g = \sqrt{\sum_{i=-M}^{M}\sum_{j=-M}^{M}\left[g(x_i',y_j')-g_{\mathrm{m}}\right]^2}. \tag{10}$$

In equations (6)–(10), $C_{\mathrm{ZNSSD}}$ presents the ZNSSD correlation criterion. In the ideal circumstance, when two subsets are identical, $C_{\mathrm{ZNSSD}}$ is zero. In application, when the value is minimized, two subsets are considered to be identical. The square size of the subset is $(2M+1)\times(2M+1)$ pixels. $f(x_i,y_j)$ presents the grey level of every pixel in the reference subset. $g(x_i',y_j')$ presents the grey level of every pixel in the deformation or the alternate-view subset. $f_{\mathrm{m}}$ presents the average grey level in the reference subset. $\Delta f$ presents the zero-mean normalization of the reference subset. $g_{\mathrm{m}}$ presents the average grey level in the deformation subset. $\Delta g$ presents the zero-mean normalization of the deformation subset.

## 3. The calibration process of 3D-DIC in tri-axial testing

Calibration plays a very important role in the accuracy of the 3D-DIC measurement. To obtain accurate measurements when performing tri-axial experiments, the special calibration process was designed to achieve three tasks: (1) undistortion: rectifying the image distortion; (2) stereo correspondence: mathematically aligning the two cameras into one viewing plane; (3) affine and projective transforms: spatial geometric transformation between the cameras and the specimen. Two types of calibration targets are applied to complete the three tasks. The checkerboard plane and the stereo calibration object are shown in figure 4. The coin and the rulers in figure 4 are used as scale references. Because the location of

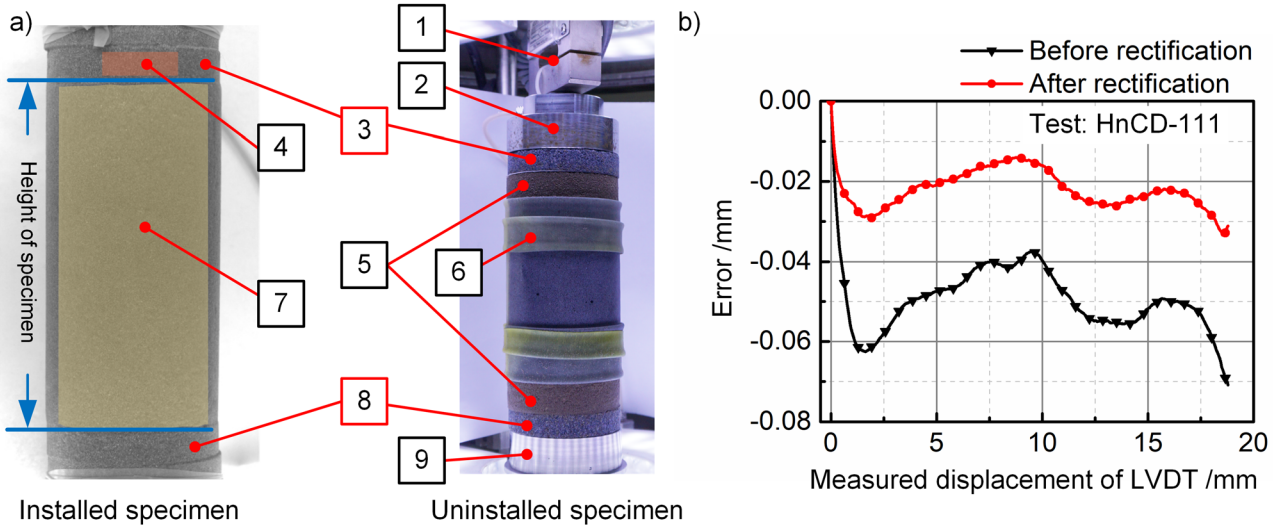


**Figure 6.** (a) The different analysis regions in the specimen and the composition of the specimen. (b) The vertical displacement error of the rectified and unrectified data. 1- loading cell; 2- loading rod; 3- top permeable stone; 4- measured loading displacement region of 3D-DIC; 5- sand specimen; 6- latex membrane; 7- measured full-field deformation region of 3D-DIC; 8- bottom permeable stone; 9- base.

the stereovision system may slightly change in every test, the calibration process must be executed before every test.

### *3.1. Undistortion of the images and stereo correspondence*

In the calibration process, the checkerboard plane shown in figure 4(a) would be orientated 28 different times in the pressure chamber. The distorted images, which include the specimen images and the calibration targets images, would be undistorted by the camera calibration algorithm based on Zhang's method [33]. The influence, which is caused by the lens distortion of two cameras and the distortion of the tempered glass in the front of the pressure chamber, is reduced. In Zhang's method, the pinhole camera model was selected to construct a mathematical model of the cameras, and a bundle adjustment has been applied to rectify the image distortion. The first task of the calibration process can be completed using Zhang's method.

According to the description in section 2, to achieve the stereovision, the rotation matrix R and translation matrix T from the right camera coordinate system to the left camera coordinate system must be obtained. According to the rectified checkerboard plane images, the position and orientation of the right camera relative to the left camera can be calculated using the bundle adjustment method. Then, the images from the two cameras relative to the left camera can be mathematically aligned into the same horizontal line (no relative rotation in 3D space). Once images of the stereovision system have been calibrated, the translation $T$ and the rotation matrix $R$ can be confirmed and can describe the location of the right camera relative to the left camera in the global coordinates, as shown in equations (3) and (4).

### *3.2. Spatial geometric transformation of the 3D reconstruction*

Once the first two tasks have been completed, the 3D morphology of the specimens can be obtained based on the 3D-DIC

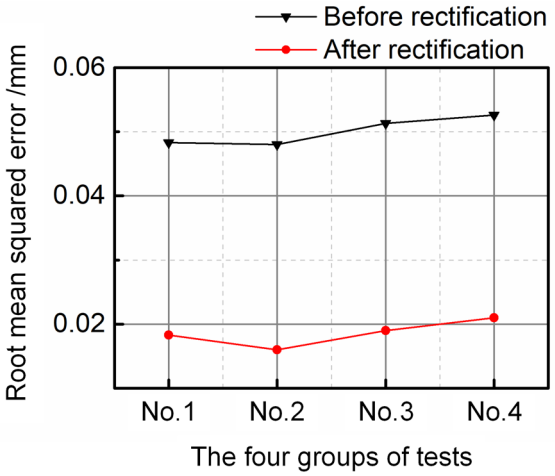


**Figure 7.** The average root-mean-squared error (RMSE) of vertical displacement in every group of tests before rectification and after rectification.

algorithm. However, the specimen relative to the stereovision system appears to be at an incline because of the different levelness and straightness between the specimen and the cameras. The 3D morphology would be at an incline relative to the stereovision system. The incline of the specimen leads to an inconvenient calculation of the shape deformation and volumetric deformation. To adjust the incline, the stereo calibration object shown in figure 4(b) is applied, which is a ceramic cylinder with a black square mark over a white background. The stereo calibration of the object is 60 mm in diameter and 120 mm in height. The distance between the two corners is 5 mm on the surface of the stereo calibration object. Before every test, the object was placed in the pressure chamber, as if it was a specimen. The image of the object was being captured by the stereovision system, and the corners in the overlap region of two cameras and the corners were detected using the Harris corner detection algorithm and subpixel accuracy algorithm, as shown in figure 5(a). Two column corners

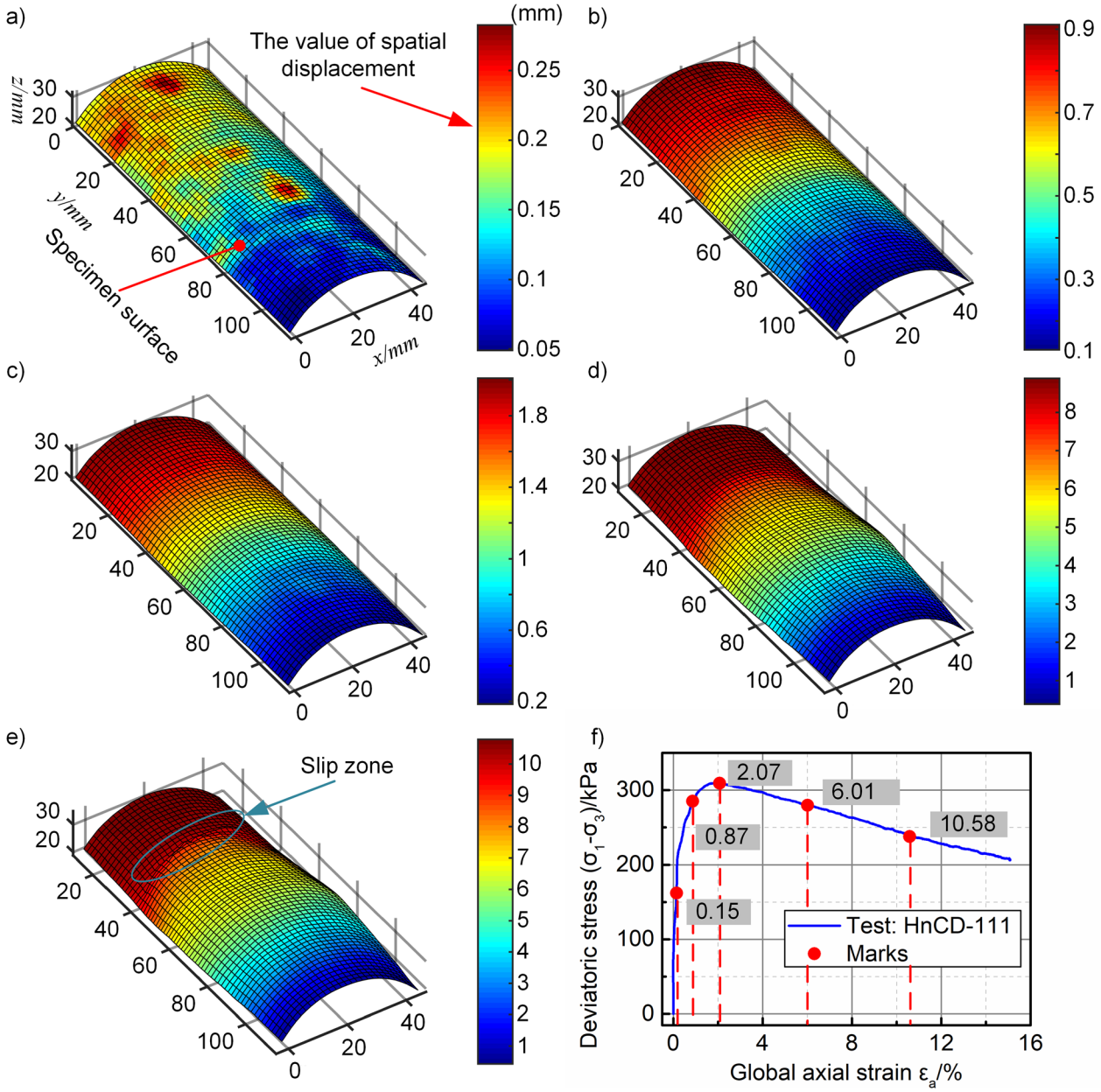


**Figure 8.** (a)–(e) The spatial displacement contours that correspond to the five moments in *f*; (f) the global stress–strain curve of HnCD-111 measured by 3D-DIC.

on the stereo calibration object are selected to fit a plane, as shown in figures 5(a) and (b). These points are axially symmetric concerning the stereo calibration object. Figure 5(b) shows the shape of the stereo calibration object composed of the raw data and the fitting plane. Obviously, the fitting plane and the surface data of the object are not parallel to the *x*-*y* plane, which is the plane of the camera system. This result indicates that the specimen base is slightly inclined relative to the stereovision system. When the specimen is placed on the specimen base, the specimen would also be inclined relative to the stereovision system. The incline of the specimen in the camera coordinate system would lead to measurement errors caused by the projective transformation.

In 3D space, two coordinate systems can be aligned with each other by rotation based on a rotation matrix, as shown in figure 5(c). To adjust the incline and to improve the accuracy of the measurement, it is necessary to obtain the rotation matrix $R_s$ from the fitting plane to the camera coordinate system. Assume $\widehat{\boldsymbol{e}}_1, \widehat{\boldsymbol{e}}_2, \widehat{\boldsymbol{e}}_3$ are the three base vectors of the fitting plane coordinate system $R_s$ can be obtained using equation (11). Through the rotation of the raw 3D data, the rectified result of the stereo calibration object is shown in figure 5(d). The rectified fitting plane is parallel to the x-y plane, and the incline of the stereo calibration object is eliminated. Compared with figure 5(b), the incline is rectified by the stereo calibration procedure:

$$\begin{bmatrix} \boldsymbol{e}_1 & \boldsymbol{e}_2 & \boldsymbol{e}_3 \end{bmatrix} = \boldsymbol{R}_s \cdot \begin{bmatrix} \widehat{\boldsymbol{e}}_1 & \widehat{\boldsymbol{e}}_2 & \widehat{\boldsymbol{e}}_3 \end{bmatrix}. \tag{11}$$

In equation (11), $\boldsymbol{e}_1$, $\boldsymbol{e}_2$, $\boldsymbol{e}_3$ are the three base vectors of the camera coordinate system: $\boldsymbol{e}_1$: (1, 0, 0); $\boldsymbol{e}_2$: (0, 1, 0); $\boldsymbol{e}_3$: (0, 0, 1).

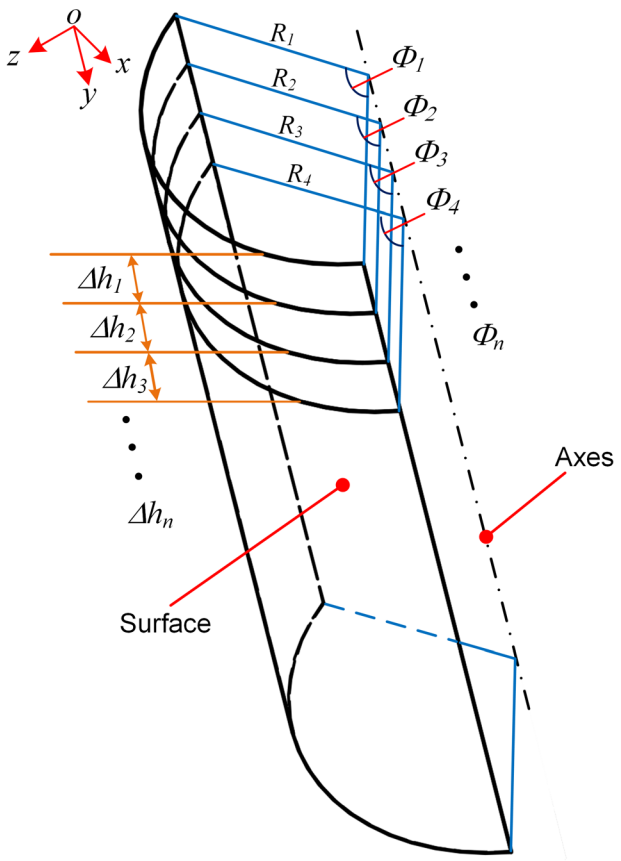


**Figure 9.** Principle for obtaining the sector cylinder volume.

$\hat{\boldsymbol{e}}_3$ is the normal unit vector of the fitting plane. $\hat{\boldsymbol{e}}_1$ and $\hat{\boldsymbol{e}}_2$ are the horizontal and vertical unit vector of the stereo calibration, respectively. $\hat{\boldsymbol{e}}_1, \hat{\boldsymbol{e}}_2, \hat{\boldsymbol{e}}_3$ in every test are listed in table 2.

### 3.3. The calibration results

Figures 5(e) and (f) present the 3D reconstruction of the initial specimen in the HnCD-111 test before rectification and after rectification, respectively. The colour bar presents the position distribution of the specimen surface in the $z$-direction. The 3D reconstruction in figure 5(e) indicates that the specimen is inclined. The specimen is rectified in figure 5(f). At the same time, the spacing between the corners on the surface of the stereo calibration object in figure 4(b) is 5 mm, and the pixel distance can be calculated by the corner recognition program. Therefore, the average physical length can be obtained, given how many millimetres a pixel represents, as listed in table 2.

After calibration and spatial geometric transformation, it is necessary to show that the calibration process is effective. The specimens are compressed by the loading rod on the top of the pressure chamber, as shown in figure 6(a). The cylindrical sand specimen was wrapped by the latex membrane, and the permeable stones were placed on the top and bottom of the specimen during the testing. The load cell has been installed in the pressure chamber for eliminating the effect of the loading rod friction. Because the strength of the specimen is far less than the range of the load cell, the vertical deformation of the loading cell was neglected. In the conventional tri-axial test, the vertical displacement of the loading rod is measured by LVDT as the vertical displacement of the specimen. Usually, LVDT has high accuracy in the linear direction and the accuracy of LVDT can reach micron scale. So, the value of LVDT is treated as the exact value in the loading direction. In order to verify the accuracy of 3D-DIC, the vertical displacement of the top permeable stone is measured by the 3D-DIC, which is in contact with the loading rod, as shown in figure 6(a) (No. 3), and the measured region of the top permeable stone is shown in figure 6(a) (No. 4, the red region). In theory, the displacement of the top permeable stone is the same as the loading rod. The vertical average value on the top permeable stone measured by 3D-DIC should equal to the vertical displacement of the loading rod measured by LVDT. In practice, due to the measurement errors, there are some differences between the values measured by LVDT and 3D-DIC. The error between 3D-DIC and LVDT was treated as the vertical displacement error of the 3D-DIC, as shown in the following equation (12). The error in HnCD-111 is shown in figure 6(b). Before rectification, the specimen relative to the stereovision system appears to be at an incline. The displacement projected on the stereovision system would become smaller than real displacement. The negative errors in figure 6(b) also reflect this situation. The effect of the spatial geometric rotation is very obvious, which reduce the errors obviously. At the same time, the average RMSEs of vertical displacement in every group of tests before rectification and after rectification also are shown in figure 7. Before rectification, the average RMSE of tests is about 0.05 mm, while the average RMSE decreases to about 0.02mm after rectification. The RMSE is obviously reduced through the rectification:

$$\text{Error} = Vd_{\text{DIC}} - Vd_{\text{LVDT}}. \tag{12}$$

In equation (12), $Vd_{\text{DIC}}$ offers the vertical displacement of the top permeable stone measured by 3D-DIC, whose displacement is equal to the loading rod. $Vd_{\text{LVDT}}$ gives the vertical displacement of the loading rod measured by LVDT.

## 4. Experimental results and discussion

### 4.1. The shape deformation of the specimen

Through the rectified procedure in the previous chapters, the 3D deformation of the specimens was obtained accurately using the 3D-DIC technique. The yellow region is the 3D-DIC measured region as shown No. 7 in figure 6(a). Figure 8 shows the progressive failure behaviours of the specimen measured using the 3D-DIC algorithm in the HnCD-111 test. Figures 7(a)–(e) present the specimen shape and spatial displacement deformation (unit: mm) contours corresponding to five moments (five red points) in the stress–strain curve, as shown in figure 8(f), which is viewed from a Euler

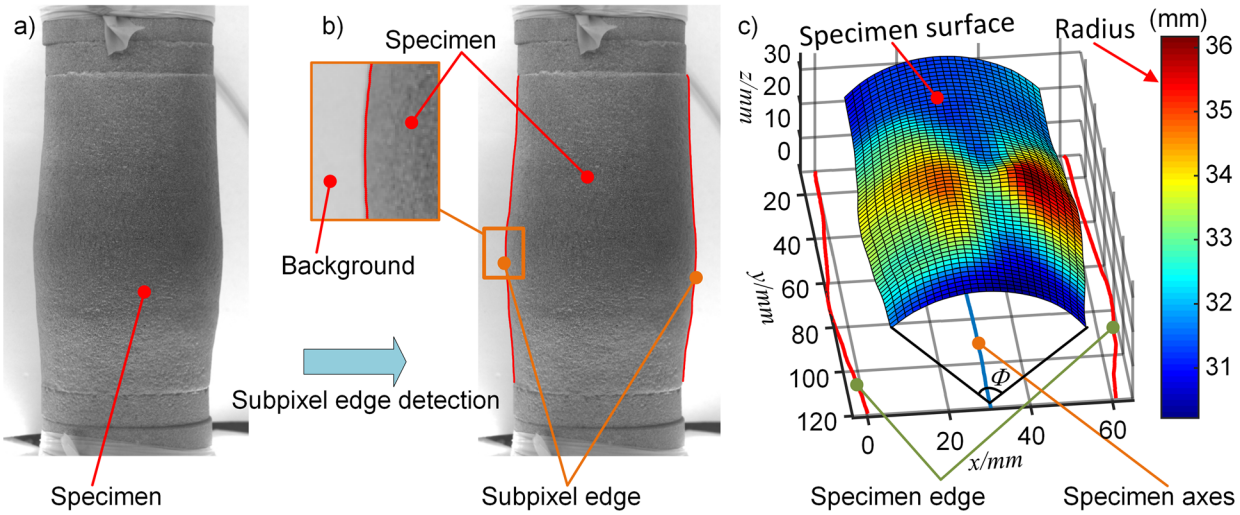


**Figure 10.** (a) The specimen at a global axial strain of 8.4% in HnCD-131; (b) the subpixel edge of the specimen; (c) the radius deformation of 3D-DIC and edge detector.

perspective. The curved surface in figure 8 shows the outline of the specimen at different moments, and the values in the colour bar present the measured displacements in space. The specimen shape changed when the specimen was compressed by the loading rod. In the initial deformation, the deformation is fairly homogeneous, and the deformation is smaller. Therefore, the shape of the specimen is almost a cylinder. With continuous loading, bulges begin to appear in the middle of the sample. The deformation of the specimen shape is very obvious. Specifically, a fracture occurred, as shown in figure 8(e). Based on the 3D-DIC technique, the full-field deformation can be obtained, and the local deformation can also be measured quantitatively during the tests. To realize the 3D measurement in tri-axial tests, the image measurement system can be easily added to the conventional tri-axial apparatus. The installation and setup of the whole system are also relatively simple, but the image measurement method can obtain more comprehensive experiment data during the tests. The method is suitable for the study of local failure and fracture in soil mechanics.

### *4.2. Volumetric strain measurement*

In order to expand the application of the image measurement in those experiments, this section would provide a method for measuring the volume strain of the specimens based on the 3D-DIC and edge detector. In this work, only a pair of cameras was used to achieve 3D measurements for a cylindrical specimen. The measurement region is the overlap area between the two cameras that covers approximately one-third of the cylindrical surface, as shown in figure 6(a) (No. 7, the yellow region). Typically, the volume of the sector cylinder can be calculated by an integral in the cylindrical coordinate system, as shown in figure 9. The height direction of the sector cylinder is evenly segmented into several layers. The area of the *n*th layer is calculated by an integral based on the radial dimension of each measured point at this layer. The volume of each layer can be obtained by the product of the area and the height of this layer. When the height, coverage angle and radius of each point in the sector cylinder are known, the volume of the sector cylinder can be obtained using equation (13):

$$V = \int_0^H \int_0^\Phi \int_0^R r \cdot \mathrm{d}r \cdot \mathrm{d}\phi \cdot \mathrm{d}h. \tag{13}$$

$H$ is the current height of the sector cylinder; $\Phi$ is the coverage angle of the measured curved surface; $R$ is the radius of each point on the sector cylinder surface.

To obtain the volume of the measured curved surface of the specimen using image measurement method, the axis of the specimen must be found, and the shape of the specimen should also be obtained. Here, combining the edge detector, a method has been proposed to obtain the specimen volume strain based on the incomplete specimen surface. In this work, the structured forests [34] have been applied to extract the boundary of the specimen. Due to the inhomogeneous deformation of the specimen, the boundary is the curve. The boundary is different than that extracted from the background. Compared to the subpixel algorithms, this edge detector based on the structure forests has achieved good results, as shown in figure 10. Figure 10(a) is the shape of the specimen at the global axial strain of 8.4% in the HnCD-131. The subpixel edges are perfectly extracted in figure 10(b). Based on the edge detector, the axes of the specimen not only can be obtained but also the diameter of the specimen can be obtained. The average diameter of the initial test is listed in table 2. Based on the initial diameter, the initial density and initial relative density can be calculated by the mass, as listed in table 1. The diameter and the axes can provide a reference for the 3D reconstruction, as shown in figure 10(c). In figure 10(c), the surface presents the shape of the specimen, and the value of the colour bar presents the radial dimension of the specimen. The surface of the specimen is very uneven, as seen in figure 10(c). Based on the integral in equation (13), the volume of the measured region can be obtained.

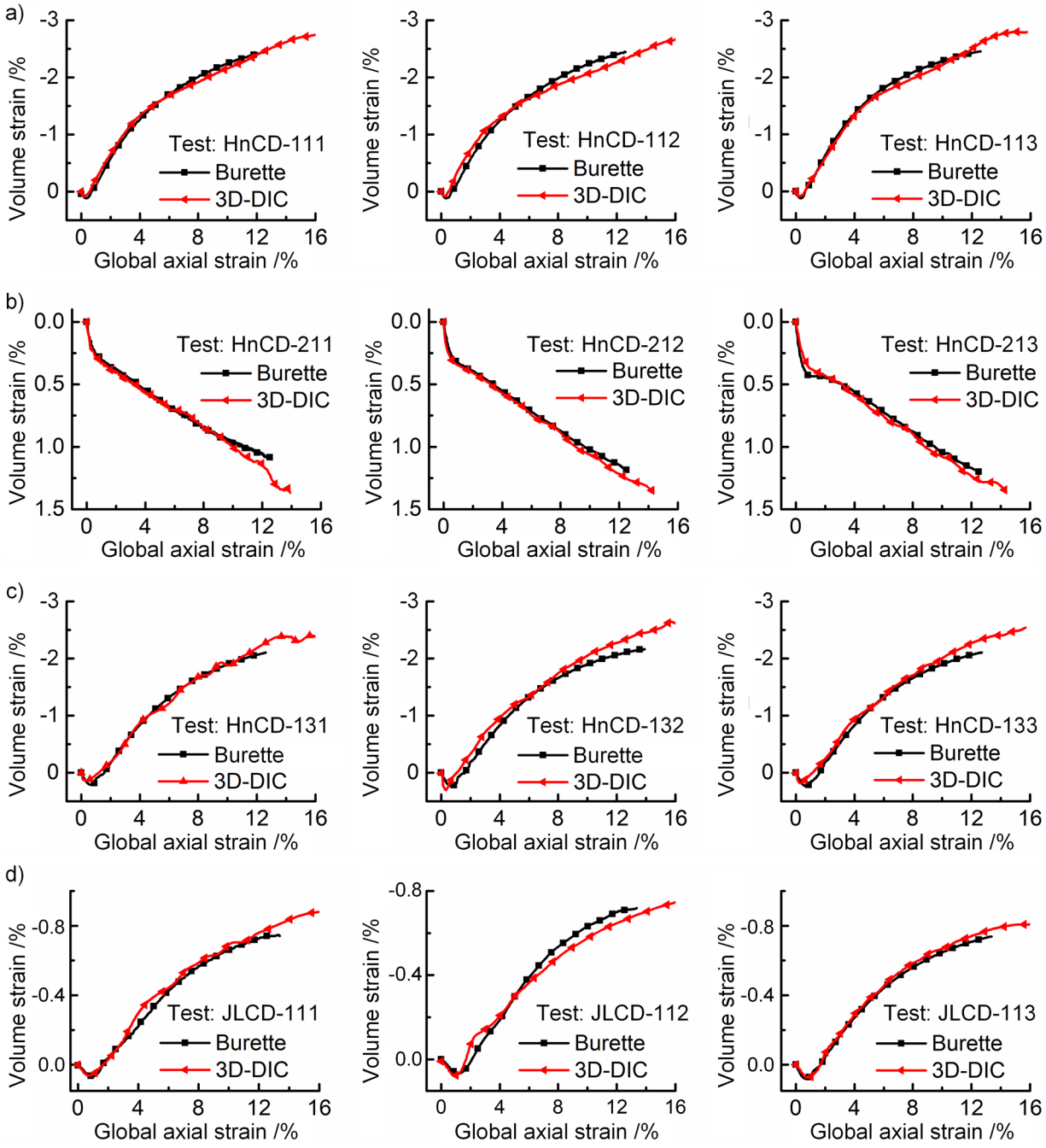


**Figure 11.** (a)–(d) The volumetric strain measured by the volume change burette and 3D-DIC in a drained condition.

In conventional saturated drained tri-axial testing, the water in the specimen can be squeezed out during the loading process. The volume change of the specimen is equal to the water discharge, which can be measured by the volume change burette. Based on the proposed method in this paper, the volume change of the measured region can also be calculated through integration theory and interpolation method. The figure 11 show that the volume strain of every test measured by proposed image measurement and measured by the volume change burette. In soil mechanics, the negative volumetric strain represents specimen expansion, and the positive volumetric strain represents specimen contraction. For sand materials in the tri-axial test, if the specimen is in a dense state, the specimen's volume would first decrease and then expand during the test. If the specimen is in a loose state, the specimen's volume would have been shrunk during the test. If the specimen is in a medium dense state, the specimen's volume may shrink or expand during the test. The results of volume deformation in figure 11 are in accordance with the above law. In figures 11(a) and (c), the sand specimens are in a dense state, which correspond to the first group of tests: HnCD-111, HnCD-112, HnCD-113; and the third group of tests: HnCD-131, HnCD-132, HnCD-133. In these tests, the specimens would be slightly shrunk in the earlier stage of the test, and the value of shrink is very small. Then the specimens' volume expanded nonlinearly during the tests. Finally,

the volume has increased by more than 2%. In figure 11(b), the sand specimens are in a medium dense state in the second group of tests: HnCD-211, HnCD-212 and HnCD-213. In these tests, the specimens' volume has been reduced during the experiments and the volume has been reduced by about 1.2% after the end of tests. The fly ash specimens are also in a medium dense state in the fourth group of tests: JLCD-111, JLCD-112 and JLCD-113. Although the curves in figure 11(d) are similar to the shape of the curves in figures 11(a) and (c), the volume changes are very small during the test. The volume has just increased by about 0.8%. The two measuring methods have the same test phenomena and good repeatability. It also proves that the local volume strain measured by 3D-DIC is reasonable. However, the measured data have some differences between the two kinds of measuring methods in the later stage of tests. The reasons are that the measuring region of 3D-DIC just covered approximately one-third of the cylindrical surface of the specimen in this work, as shown No. 7 in figure 6(a) and the specimens have serious inhomogeneous deformation in the later stage of tests. The inhomogeneous deformation becomes more and more obvious during the test. For inhomogeneous specimens, there would be a deviation in the results measured by 3D-DIC. But the deviation mainly occurred in the later stage of the tests, and the values are small. Due to the soil specimen's randomness, it is necessary to use repeated tests to verify the stability of the results in geotechnical test. Compared to the results of the volume change burette, the results in the same group also prove that the local volume strain measured by the proposed method are reasonable and stable. Because every specimen would have randomness in the preparation process and the surface of each specimen would be slightly different, the results measured by image measurement and burette are also some differences in the same group, but the similar results already indicate that the properties of the specimens are similar in the same group.

Based on the image measurement results, the local volume and local volume strain in the measured region all can be obtained, while the conventional method can only obtain the global volume change. Through the repetitive tests, these results are sufficient to prove the accuracy and stability which are measured by 3D-DIC and rectified by the proposed calibration method. The local volume change and local deformation filed can be accurately obtained using the 3D-DIC and edge detector. The proposed method would help to provide more comprehensive data to research the local failure in soil mechanics.

## 5. Conclusion

In this paper, a geotechnical tri-axial apparatus that can be combined with a digital image measurement system was developed independently in our laboratory. At the same time, a 3D-DIC algorithm, which combines incremental RG-DIC, has been applied to measure the large full-field deformation of soil specimens in tri-axial testing. More importantly, the proposed calibration procedure has been used to solve the problem for the effect of the projective transformation in image measurement. The measurement error can be obviously decreased after the calibration procedure. In order to expand the application of the 3D-DIC in those experiments, combined with a subpixel edge detector, the volume strain can be calculated based on the incomplete 3D specimen surface. A series of tri-axial compressive tests were performed. The results from the image measurement were similar to than the results from the conventional method, which can prove the effectiveness of the proposed method. However, the local volume and local volume strain of the specimen cannot be obtained using the conventional method, while the digital image system can determine these values. By comparing the conventional method, the results of the proposed method are shown to be accurate. Using the method in this paper, the soil specimen 3D total, local strain deformation, and volume changes during tri-axial testing can be measured accurately. The results can provide more information for the establishment of constitutive models in soil mechanics. The accuracy of the measurement results is verified in saturated soil specimens in this paper. The proposed image measurement method can be applied to many kinds of soil mechanics tests, example for the unsaturated soil test. Water and air would be contained in the unsaturated soil specimen. The volume change cannot be obtained by the conventional draining water method. So, the proposed method would be applied to unsaturated soil specimens to obtain its parameters.

## Acknowledgments

This work was supported by the National Natural Science Foundation of China (Grant Nos. 51975082 and 51309047).

## ORCID iDs

Pengpeng Wang https://orcid.org/0000-0002-4743-0046
Yong Sang https://orcid.org/0000-0001-7743-1819
Xiaoxia Guo https://orcid.org/0000-0001-8237-904X
Longtan Shao https://orcid.org/0000-0002-2806-4052
Jianlong Zhao https://orcid.org/0000-0002-3788-3930
Xiaomeng Ji https://orcid.org/0000-0002-7173-5464

## References

[1] Peters W, Ranson W, Sutton M, Chu T and Anderson J 1983 Application of digital correlation methods to rigid body mechanics *Opt. Eng.* **22** 738–42
[2] Sutton M, Wolters W, Peters W, Ranson W and McNeill S 1983 Determination of displacements using an improved digital correlation method *Image Vis. Comput.* **1** 133–9
[3] Pan B, Li K and Tong W 2013 Fast, robust and accurate digital image correlation calculation without redundant computations *Exp. Mech.* **53** 1277–89
[4] Gao Y, Cheng T, Su Y, Xu X, Zhang Y and Zhang Q 2015 High-efficiency and high-accuracy digital image correlation for three-dimensional measurement *Opt. Lasers Eng.* **65** 73–80

[5] Neggers J, Blaysat B, Hoefnagels J and Geers M 2016 On image gradients in digital image correlation *Int. J. Numer. Methods Eng.* **105** 243–60

[6] Grédiac M, Blaysat B and Sur F 2017 A critical comparison of some metrological parameters characterizing local digital image correlation and grid method *Exp. Mech.* **57** 871–903

[7] Huang J, Zhang L, Jiang Z, Dong S, Chen W, Liu Y, Liu Z, Zhou L and Tang L 2018 Heterogeneous parallel computing accelerated iterative subpixel digital image correlation *Sci. China Technol. Sci.* **61** 74–85

[8] Yuan Y, Zhan Q, Xiong C and Huang J 2017 Digital image correlation based on a fast convolution strategy *Opt. Lasers Eng.* **97** 52–61

[9] Hartmann C, Wang J, Opristescu D and Volk W 2018 Implementation and evaluation of optical flow methods for two-dimensional deformation measurement in comparison to digital image correlation *Opt. Lasers Eng.* **107** 127–41

[10] Pan B, Qian K, Xie H and Asundi A 2009 Two-dimensional digital image correlation for in-plane displacement and strain measurement: a review *Meas. Sci. Technol.* **20** 062001

[11] Zhan Q, Yuan Y, Fan X, Huang J, Xiong C and Yuan F 2016 Digital image correlation involves an inverse problem: A regularization scheme based on subset size constraint *Opt. Lasers Eng.* **81** 54–62

[12] Yuan Y, Huang J, Peng X, Xiong C, Fang J and Yuan F 2014 Accurate displacement measurement via a self-adaptive digital image correlation method based on a weighted ZNSSD criterion *Opt. Lasers Eng.* **52** 75–85

[13] Skarżyński Ł, Kozicki J and Tejchman J 2013 Application of DIC technique to concrete—study on objectivity of measured surface displacements *Exp. Mech.* **53** 1545–59

[14] Motamedinia H, Hataf N and Habibagahi G 2018 A study on failure surface of helical anchors in sand by PIV/DIC technique *Int. J. Civ. Eng.* 1–15

[15] Blaber J, Adair B S and Antoniou A 2015 A methodology for high resolution digital image correlation in high temperature experiments *Rev. Sci. Instrum.* **86** 035111

[16] Campo A, Klosiewicz P and Dirckx J 2015 Digital image correlation for full-field high resolution assessment of leaf growth *J. Plant Growth Regul.* **34** 433–9

[17] Sang Y, Zhao J, Duan F, Sun W and Zhao H 2018 A novel automatic device to measure deformation inside transparent soil based on DIC technology *Meas. Sci. Technol.* **30** 035202

[18] Sutton M A, Orteu J J and Schreier H 2009 *Image Correlation for Shape, Motion and Deformation Measurements: Basic Concepts, Theory and Applications* (Berlin: Springer) (https://doi.org/10.1007/978-0-387-78747-3)

[19] Chen F, Chen X, Xie X, Feng X and Yang L 2013 Full-field 3D measurement using multi-camera digital image correlation system *Opt. Lasers Eng.* **51** 1044–52

[20] Yu J H, McWilliams B A and Kaste R P 2016 Digital image correlation analysis and numerical simulation of aluminum alloys under quasi-static tension after necking using the Bridgman's correction method *Exp. Tech.* **40** 1359–67

[21] Xue Y, Cheng T, Xu X, Gao Z, Li Q, Liu X, Wang X, Song R, Ju X and Zhang Q 2017 High-accuracy and real-time 3D positioning, tracking system for medical imaging applications based on 3D digital image correlation *Opt. Lasers Eng.* **88** 82–90

[22] Shao X, Dai X, Chen Z, Dai Y, Dong S and He X 2016 Calibration of stereo-digital image correlation for deformation measurement of large engineering components *Meas. Sci. Technol.* **27** 125010

[23] Medina-Cetina Z and Rechenmacher A 2010 Influence of boundary conditions, specimen geometry and material heterogeneity on model calibration from triaxial tests *Int. J. Numer. Anal. Methods Geomech.* **34** 627–43

[24] Tang Y, Okubo S, Xu J and Peng S 2019 Progressive failure behaviors and crack evolution of rocks under triaxial compression by 3D digital image correlation *Eng. Geol.* **249** 172–85

[25] Higo Y, Oka F, Sato T, Matsushima Y and Kimoto S 2013 Investigation of localized deformation in partially saturated sand under triaxial compression using microfocus x-ray CT with digital image correlation *Soils Found.* **53** 181–98

[26] Wang P, Sang Y, Shao L and Guo X 2019 Measurement of the deformation of sand in a plane strain compression experiment using incremental digital image correlation *Acta Geotech.* **14** 547–57

[27] Song A, Medina-Cetina Z and Rechenmacher A L 2012 Local deformation analysis of a sand specimen using 3D digital image correlation for the calibration of a simple elasto-plastic model *Geocongress* pp 2292–301

[28] Pan B, Dafang W and Yong X 2012 Incremental calculation for large deformation measurement using reliability-guided digital image correlation *Opt. Lasers Eng.* **50** 586–92

[29] Li L and Zhang X 2019 Factors influencing the accuracy of the photogrammetry-based deformation measurement method *Acta Geotech.* **14** 559–74

[30] ASTM 2011 *D7181-11: Method for Consolidated Drained Triaxial Compression Test for Soils* (Conshohocken, PA: ASTM International: West)

[31] Chen Y, Wei J, Huang H, Jin W and Yu Q 2018 Application of 3D-DIC to characterize the effect of aggregate size and volume on non-uniform shrinkage strain distribution in concrete *Cement Concrete Comp.* **86** 178–89

[32] Pan B, Xie H and Wang Z 2010 Equivalence of digital image correlation criteria for pattern matching *Appl. Opt.* **49** 5501–9

[33] Zhang Z 2000 A flexible new technique for camera calibration *IEEE Trans. Pattern Anal. Mach. Intell.* **22** 1330–4

[34] Dollár P and Zitnick C L 2015 Fast edge detection using structured forests *IEEE Trans. Pattern Anal. Mach. Intell.* **37** 1558–70